Synthesis of Fe-filled carbon nanocapsules by an electric plasma discharge in an ultrasonic cavitation field of liquid ethanol

Ruslan Sergiienko,[a] Etsuro Shibata, Zentaro Akase, Hiroyuki Suwa, Daisuke Shindo, and Takashi Nakamura
Institute of Multidisciplinary Research for Advanced Materials, Tohoku University, Aobaku, Sendai 980-8577, Japan

(Received 30 April 2006; accepted 12 July 2006)

Nanoparticles of iron carbides (Fe_3C and χ-$Fe_{2.5}C$) wrapped in multilayered graphitic sheets were synthesized by a developed method in which an electric plasma was generated in an ultrasonic cavitation field containing thousands of tiny activated bubbles in liquid ethanol. Annealing changed the phase composition, structure, and size of the carbon nanocapsules as most of the iron carbides decomposed into the α-Fe phase and graphite. Powder samples annealed at 873 and 973 K have maximal saturation magnetization values equal to 80.6 and 83.4 A m^2/kg, respectively, which is approximately 40% of the value of bulk iron. Using this method, it will be possible to synthesize nanoparticles of a metal of choice encapsulated by graphite shells by selecting appropriate materials for the ultrasonic tip and electrodes.

I. INTRODUCTION

There has been an increasing interest in recent years in the development of new nanoscale magnetic materials for recording media in computer technology,[1] biomedical,[2] and other applications. The magnetic nanoparticles of 3d metals (iron, nickel, and cobalt) coated with crystalline graphite shells, called "carbon nanocapsules," are examples of such interesting materials. The coating helps to prevent the aggregation and environmental degradation of the metallic cores. To date, carbon-coated nanocapsules have been synthesized by a conventional arc discharge[3] and a modified arc discharge[4] in a gaseous atmosphere. Before undergoing arc vaporization, the metal (or metal oxide) precursors are normally packed inside a cavity drilled into a graphite electrode. However, this method requires expensive vacuum equipment and high electric power for the generation of the arc discharge.

A synthetic method for producing iron carbide nanoparticles wrapped in multilayered graphitic shells has been demonstrated previously in an experiment using liquid ethanol.[5] This method takes advantage of the fact that an electric plasma can be generated and maintained in an organic liquid under ultrasonic irradiation. Ultrasonic cavitation causes a very highly localized high temperature and pressure region where tiny bubbles are collapsing—a region referred to as a so-called "hot spot."[6–8] An ultrasonic cavitation field, with its many activated tiny bubbles, enhances electrical conductivity because of the radicals and free electrons formed within it. Thus, an electric plasma discharge can be generated at a remarkably low voltage, such as 55 V DC, even in insulating organic liquids such as benzene and ethanol.[5,9,10] Without the ultrasonic irradiation, no plasma discharge can take place at such low electric power levels. Usually, a transient high voltage is necessary to generate the plasma discharge in a neutral medium. Breakdown voltages for the generation of plasma discharge in gaseous phases such as air, oxygen, and nitrogen can be derived according to Paschen's law.[11] These voltages are very high, usually several hundred volts, whereas the electric breakdown voltages of liquid hydrocarbons are several tens of kilovolts.[12,13] Thus, in contrast to traditional arc discharge units requiring a high-power electric system and expensive vacuum equipment, a plasma discharge produced under conditions of low electric power with ultrasonic irradiation has a cost advantage and the potential to be applied for continuous liquid-phase processing of functional nanocarbon materials, even in organic liquids.

The objective of the present work was to use this method to synthesize iron nanoparticles with graphitic coatings. Liquid ethanol was used as the organic liquid

[a] Address all correspondence to this author.
e-mail: ruslan@mail.tagen.tohoku.ac.jp
DOI: 10.1557/JMR.2006.0316

for experiments. However, iron is a strong carbide-forming element, and its vapors in the plasma reacted with carbon from decomposed ethanol molecules to form iron carbides. Therefore, in the as-prepared powder sample (before annealing), iron carbide nanoparticles (in particular, Fe_3C and χ-$Fe_{2.5}C$) were observed, covered by graphite shells. To transform the iron carbides into the α-Fe phase and improve the magnetic properties, the samples were annealed at different temperatures.

Here, transmission electron microscopic (TEM) observations are reported and discussed, along with the x-ray diffractometer (XRD) analysis of carbon encapsulated iron and iron carbide nanoparticles, as well as their magnetic properties. The mechanism of carbon nanocapsules formation proposed in Ref. 5 is examined in more detail using results from a plasma spectroscopic system.

II. EXPERIMENTAL

In this study, we exploited the same experimental apparatus as presented in Ref. 5 with the addition of an optical probe to investigate the emission spectrum from the plasma discharge. Figure 1 shows a schematic diagram of the experimental apparatus and the variation of current and voltage during the process of plasma discharge. An iron tip (diameter 18 mm, purity 99.9%) was fixed on the top of a titanium ultrasonic horn. Placing such a tip on the horn does not reduce the efficiency of the ultrasonic irradiation significantly. Two iron electrodes (diameter 2 mm, purity 99.7%) were inserted 1 mm apart from each other just beneath but very close to the iron tip fixed on the ultrasonic horn. During the experiment, the electrodes and the bottom of the iron tip were consumed by thermal evaporation. An ultrasonic homogenizer (US-600NCVP; Nissei, Tokyo, Japan) was used at 600 W and 20 kHz in the experiments to irradiate 100 mL of liquid ethanol (S-grade; Wako, Osaka, Japan) in a glass vessel. The glass vessel was cooled using an ice bath, and was sealed with a Teflon lid. An Ar gas flow was directed into it to maintain an inert atmosphere. During the irradiation, the voltage on the electrodes was kept at 55 V using a constant voltage power unit (AD-8735; A&D, Tokyo, Japan), and the upper current limit of the unit was set at 1.58 A.

An electric plasma was generated in the cavitation field just beneath the horn. The electrode current became momentarily higher than the current limit of the power unit when the plasma discharge occurred, as shown in Fig. 1(b). The plasma flashed from the intermittent decrease of the voltage when the current exceeded the limit of the power unit. However, without ultrasonic irradiation, no plasma was generated using just the electric power supply. When the plasma flashes became infrequent from the wear of the electrodes and the bottom

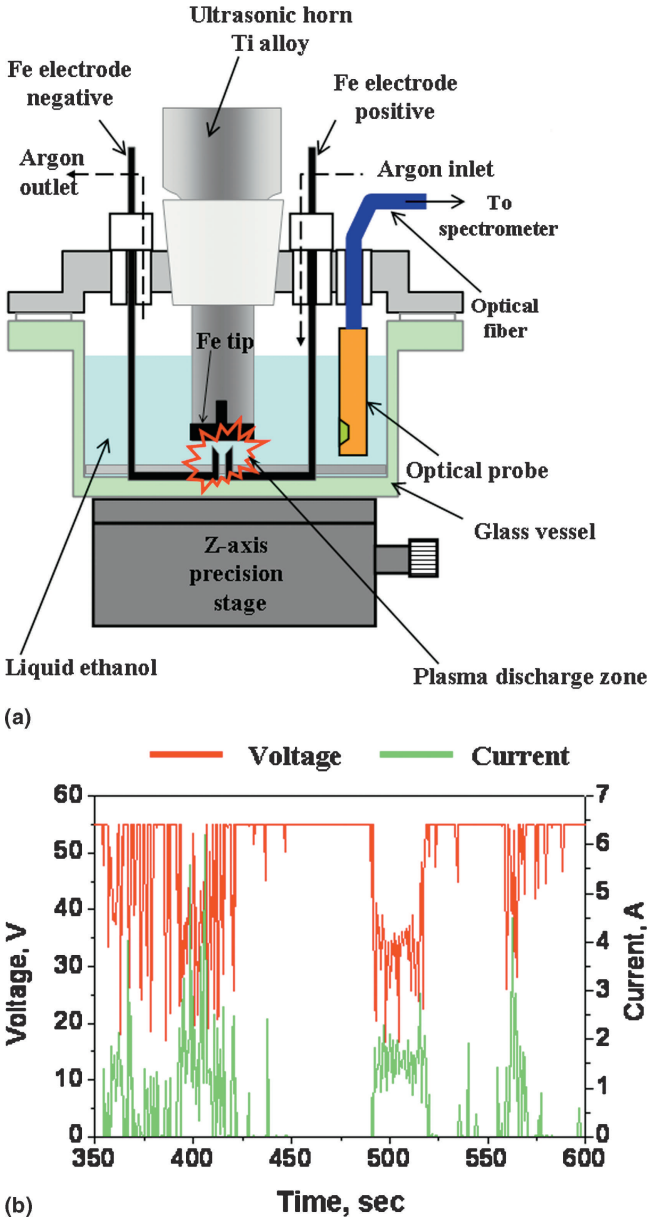

FIG. 1. (a) Schematic diagram of the experimental apparatus and (b) variation of plasma discharge current and voltage during the experiment.

surface of the ultrasonic horn, the position of the electrodes was raised using the *Z*-axis precision stage. The rack-mounted ultrasonic horn was transferred up and down by means of a screw gear independent of the glass vessel. To diagnose the plasma discharge, we designed a spectroscopic system (Fig. 1) that enabled us to measure the plasma emission spectrum in the wavelength range from 200–850 nm. Optical emission from the plasma discharge was collected using an optical probe immersed in the ethanol and transmitted via an optical fiber to a USB 2000 spectrometer connected to a computer. The

emission spectrum provided useful additional information to gain a better insight into the mechanism of carbon nanocapsule formation.

After a 1-h experiment, the carbonaceous powder produced was separated by centrifugation from the remaining liquid ethanol, and was then etched in a 15% HCl solution for 24 h at 313 K to remove excess exposed iron particles. After subsequent drying in a vacuum at 313 K, the powder samples were put in a platinum pan and annealed in pure Ar (purity 99.99995%) at various temperatures (573, 673, 773, 873, 973, 1073, and 1173 K) for 2 h. Before admission of the inert gas, the annealing tube was evacuated by a rotary pump. After being suspended in ethanol, the resulting powder was dropped onto a copper microgrid covered with amorphous carbon film and dried in preparation for the 300 kV TEM (JEM-3010) investigations. The TEM observations allowed a determination of the overall morphology of the powder samples and the structures of the carbon nanocapsules, before and after annealing. Also, TEM micrographs were used to measure the particle size distribution. Some of the nanocapsules were examined by means of selected-area electron diffraction patterns and digital diffractograms, which were obtained by a fast Fourier transformation (FFT) of digitized high-resolution TEM (HRTEM) images. To identify the elemental composition of the carbon nanocapsules, an energy dispersive x-ray study was carried out.

The phases of all samples were surveyed with an XRD using CuK_{α} radiation at room temperature (RINT2000; Rigaku Instruments, Tokyo, Japan). A vibration sample magnetometer (VSM) operating at room temperature with an applied magnetic field up to 1200 kA/m (TOEI VSM-5-18) was used to measure the magnetic properties of the as-prepared and annealed powder samples. For the VSM measurements, specimens of the synthesized powder samples containing the carbon nanocapsules and amorphous carbon with a weight of 6–15 mg were immobilized using paraffin in a small diameter plastic cell.

III. RESULTS AND DISCUSSION

A. Structure and morphology of the carbon nanocapsules

Random TEM scans of areas on the sample grid produced images typical of those shown in Fig. 2 for an as-prepared sample [Fig. 2(a)], and those annealed at different temperatures [Figs. 2(b)–2(d)]. The particles observed in the as-prepared sample [Fig. 2(a)] and that annealed at 673 K [Fig. 2(b)] are nearly spherical in shape. Many of the carbon nanocapsules annealed at temperatures higher than 873 K [Figs. 2(c) and 2(d)] are far from spherical, and some of them have a polyhedral form, as shown later in Figs. 5(b) and 5(c).

Figure 2 also shows that after annealing at elevated temperatures, the nanoparticles became larger because of the tendency of the system to decrease its surface energy. Such a decrease is possible only by reducing the total surface of the particles by sintering of small particles into larger ones.

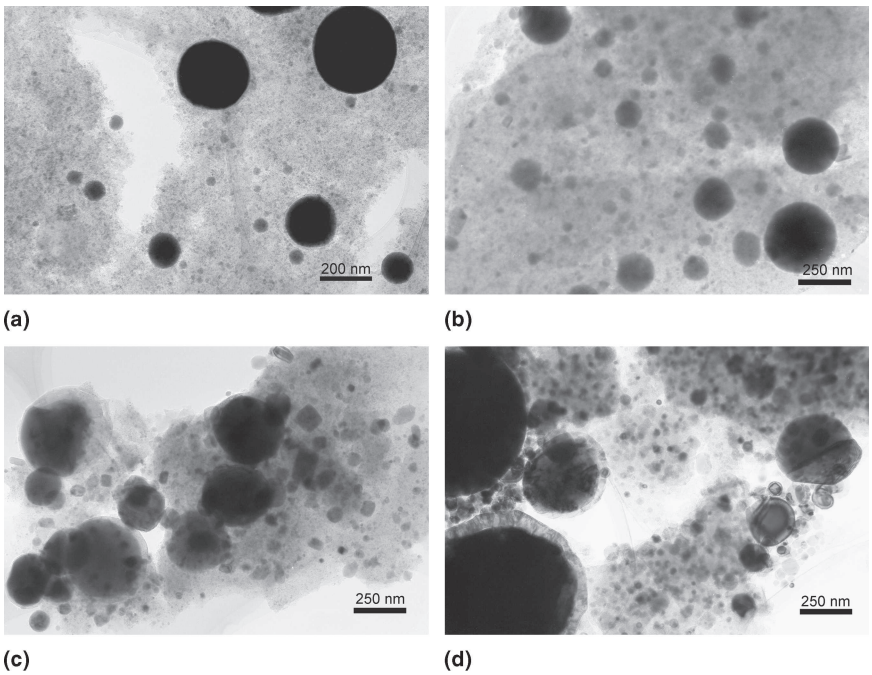

FIG. 2. (a) Typical TEM images of the as-prepared carbon nanocapsules, and after annealing in Ar for 2 h at (b) 673 K, (c) 873 K, and (d) 1173 K.

By measuring the approximate diameters of more than 1500 particles in TEM micrographs taken at different magnifications, the size distribution of the nanocapsules in each sample was obtained. Histograms of the external diameters of the carbon nanocapsules are given in Fig. 3. The use of semi-logarithmic histograms [Figs. 3(a) and 3(c)] better shows the relative number of very large and small particles in a single figure. For the unannealed sample, Fig. 3(a) shows that although the nanoparticles' diameters ranged from several nanometers to as large as 650 nm, particles smaller than 20 nm occurred most frequently. In fact, nanoparticles smaller than 10 nm in diameter constituted by far the majority, about 96.5% of the total. The fraction of particles larger than 100 nm was about 0.01%; however, their contribution to the total volume of the particles was much greater than that of the small (<10–20 nm) nanoparticles. The linear histogram in Fig. 3(b), singly plotted for small particles, shows that the 3–13 nm is the most common particle diameter for the as-prepared sample.

After annealing at 873 K, the particles became larger [Figs. 3(c) and 3(d)]; the mean size of small carbon nanocapsules had increased to 25 nm [Fig. 3(d)]. The number of particles with diameters larger than 100 nm [Fig. 3(c)] increased significantly from sintering. In addition, the upper size limit increased from about 650 nm in the unannealed sample to 1200 nm in the annealed nanocapsules.

Typical morphologies of the as-prepared carbon nanocapsules were shown in an earlier article.[5] The crystalline carbide (orthorhombic Fe_3C and monoclinic χ-$Fe_{2.5}C$ structures) cores are spherical in shape and covered with carbon layers. During the analysis, spherical carbon nanocapsules with an amorphous core were also found in as-prepared samples. Elemental analyses[5] of the carbon nanocapsules showed that iron and carbon were the only elements present.

In addition to increasing the particle size, annealing of the powder at different temperatures produced changes in the phase composition and structure of the carbon nanocapsules. Iron carbides are unstable compounds and decompose at well-defined temperatures into pure iron (α-Fe or γ-Fe, depending on whether the temperature is above or below 1000 K) and graphite.[14] TEM observations of the cores of the spherical carbon nanocapsules annealed at 673 K for 2 h showed that most of them had an orthorhombic Fe_3C structure (image not shown here). Cores with the α-Fe phase were seldom observed because a temperature of 673 K is insufficient for complete decomposition of the cementite. After annealing at 673 K for 2 h, χ-$Fe_{2.5}C$ cores could not be found, presumably because this monoclinic structure was converted into cementite.

At higher annealing temperatures (873 K and above for 2 h), the iron carbides were almost completely transformed into the α-Fe phase, except for the cores of small-sized nanocapsules (<10–20 nm), which remained as cementite. Figures 4(a) and 4(b) show the TEM image and corresponding selected-area electron diffraction pattern of a typical metallic iron particle covered with graphitic

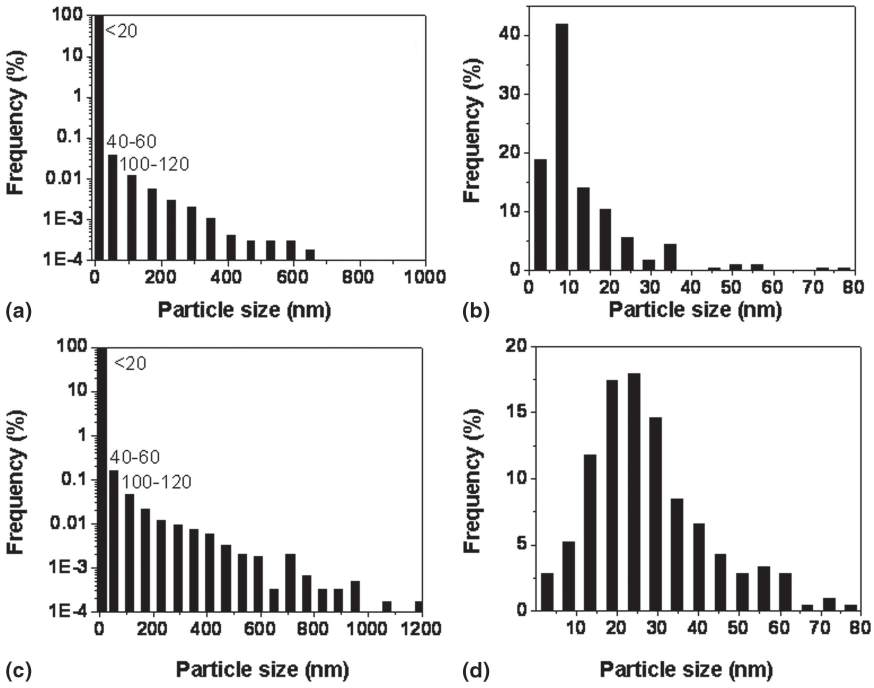

FIG. 3. Distribution of carbon nanocapsules external diameters: (a) and (b) as-prepared sample; (c) and (d) after annealing in Ar for 2 h at 873 K.

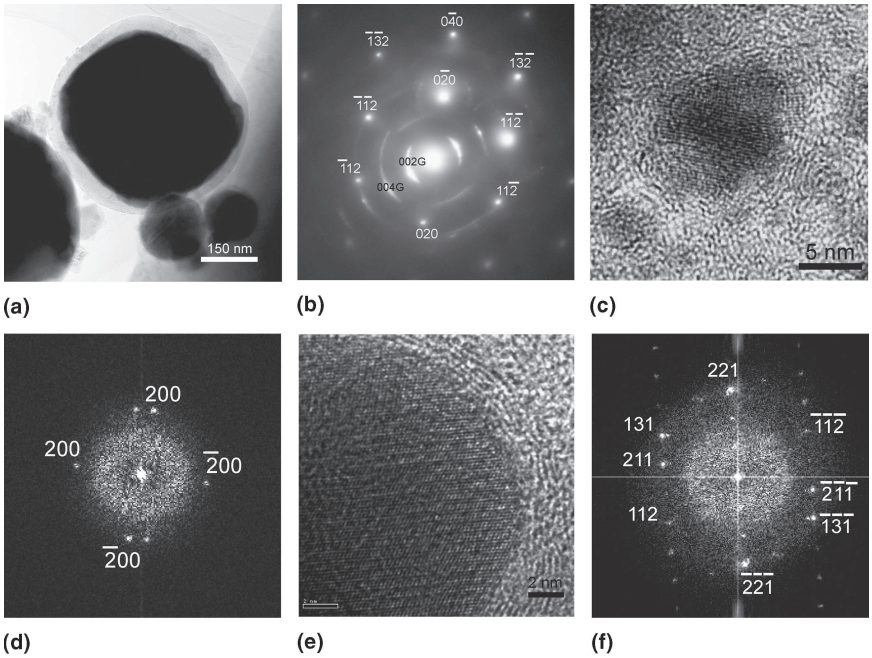

FIG. 4. (a) TEM image of an α-Fe particle and (b) the corresponding selected area electron diffraction pattern from the core of α-Fe annealed at 873 K for 2 h in Ar. The Miller index indicated by G is for the graphitic carbon. (c) and (e) HRTEM images, and (d) and (f) the corresponding digital diffractograms computed by FFT of the crystalline cementite cores annealed at 873 and 1173 K, respectively for 2 h in Ar.

carbon after annealing at 873 K. The diffraction spots [Fig. 4(b)] originating from the crystalline core coincide with those expected for the [201] zone-axis pattern from α-Fe with a body-centered cubic structure and arcs originating from the outer graphitic carbon. No intermediate phases were observed between the core of pure iron and the outside graphite layers. Thus, the morphology presented here for the large (>20 nm) nanocapsules is quite similar to that of nanocapsules obtained by the common arc-discharge method[3,4]; i.e., spherical shapes with tightly wrapped graphitic layers.

Carbon nanocapsules smaller than 10–20 nm in diameter were observed in samples before[10] and after annealing, although the number of these particles in the annealed samples was decreased, especially after sintering at 1173 K. Images of the annealed cementite cores of nanocapsules smaller than, or around, 10–20 nm in size with incomplete graphite layers are presented in Figs. 4(c) and 4(e). The spacing of the lattice fringes of these layers is still about 0.34 nm, which is close to that of graphite (002) planes. In size and form, these small carbon nanocapsules resemble those synthesized by the cosputtering of Co, Ni, and graphite in argon gas with subsequent thermal annealing in a vacuum.[15,16] To clarify the structure of these encapsulated nanoparticles, the digital diffractograms were obtained by FFT from the HRTEM images presented in Figs. 4(c) and 4(e). In spite of a high temperature annealing at 873–1173 K, the majority of the small-sized cores remained as cementite, although it cannot be denied that some were transformed into α-Fe. The digital diffractogram from the 873 K anneal [Fig. 4(d)] clearly shows the diffraction spots from the crystalline core with an interplanar distance of 2.54 A. This distance is close to the one between the (200) lattice plane of cementite. The digital diffraction pattern with the array of spots [Fig. 4(f)] produced from the HRTEM image [Fig. 4(e)] of an 1173 K annealed carbon nanocapsule (external diameter about 20 nm, and thickness of the shell approximately 2–3 nm) can be ascribed to a single Fe_3C crystallite. There is good reason to believe that the surface of small-sized nanoparticles plays a key role in the decomposition of the cementite, as with decreasing particle size, the surface energy rises significantly, and this can lead to an increase in the free energy of transformation of cementite nanoparticles into α-Fe.

After annealing at 1173 K, most of the graphitic shells were not distributed with a uniform thickness over the surface of the nanoparticles, as shown in Fig. 5(a), and the shapes of the nanocapsules were far from spherical [Fig. 5(b)]. In rare instances, we found polyhedral cores nesting in a thick-layered material with a cavity inside, as shown in Fig. 5(c). The sequence of diffraction spots taken from the polyhedral core shown in Fig. 5(c) is attributable to α-Fe [Fig. 5(d)]. During the high-temperature annealing, empty polyhedral shells of carbon were seldom observed (not shown here). TEM analysis confirms that these polyhedral shells consist of graphitic layers. This type of structure was found only in the samples annealed at the highest temperature of 1173 K.

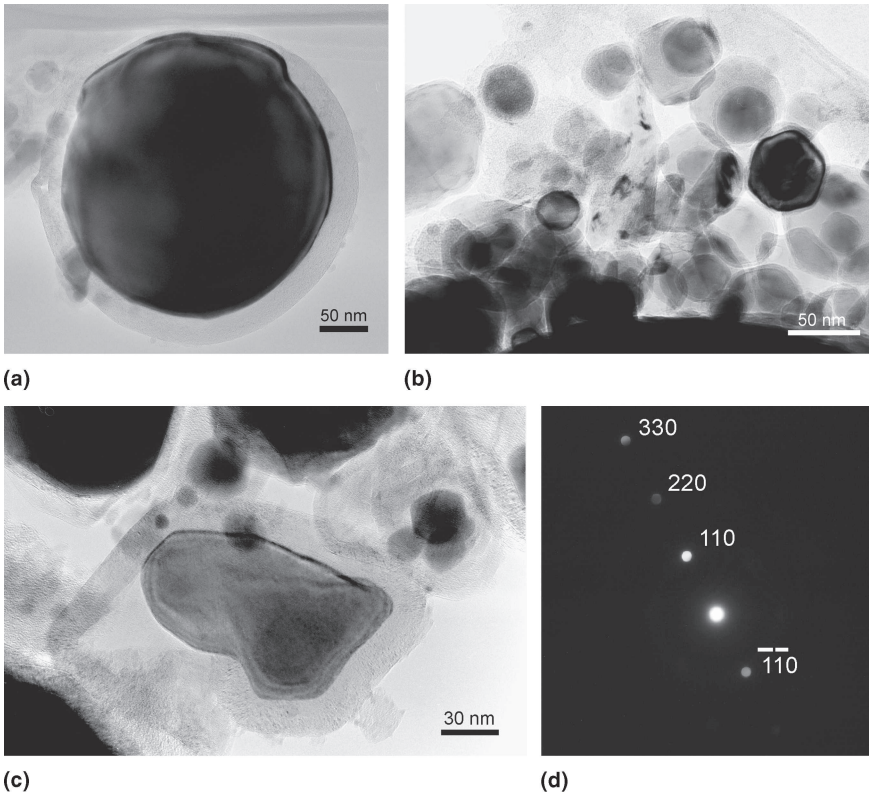

FIG. 5. (a) TEM image of an α-Fe particle wrapped in nonuniform thickness multilayered graphitic shell. (b) TEM image of carbon nanocapsules with different shapes nesting in graphitic shells. (c) TEM image of a polyhedral α-Fe core nesting in thick-layered material with a cavity inside. (d) The corresponding microdiffraction pattern from the polyhedral crystalline core depicted in (c). The samples were annealed in Ar at 1173 K for 2 h.

Examination of this structural phenomenon suggests that the cores were ejected out through the opened holes or incomplete closures of the outer graphitic shells and the empty shells were left behind. The reason for the ejection might involve the sintering tendency of the metal particles.[4]

Annealing intensified the graphitization of the surrounding layer from iron carbide decomposition. TEM observations showed that the number of graphitic layers in the as-prepared carbon nanocapsules ranged from 3 to 40, depending on the particle size; and with an increase in the annealing temperature, the thickness of the graphite shell increased. Small particles (less than 10–20 nm in diameter) like those shown in Figs. 4(c) and 4(e) regardless of annealing, were covered by several layers of graphite (thickness was about 1.5–3 nm), whereas large particles had about 40 layers[5] (thickness was about 13 nm) of graphite encasing them. Some of the large carbon nanocapsules (>250 nm in diameter) annealed at 873–1173 K were covered by 70–120 layers as thick as 25–40 nm [Figs. 4(a) and 5(a)].

In addition to the α-Fe phase of iron stable at room temperature, the high-temperature phase γ-Fe, was also occasionally found in the samples annealed at high temperatures (873–1173 K). In addition, in the samples annealed at high temperatures, small quantities of particles with an oxidized shell composed of Fe_3O_4 were observed (less than one-hundredth of the amount of α-Fe particles with graphite shells).

B. Investigation of carbon nanocapsules formation by optical emission spectroscopy

An emission spectrum from the plasma discharge of pure ethanol, iron electrodes, and tip, used to provide an explanation of carbon nanocapsule formation, is shown in Fig. 6. The dominant lines are the Balmer line of atomic hydrogen $H_\alpha g$ ($\lambda = 656.27$ nm), Swan bands system of C_2 molecules ($\lambda = 516.52$, 558.55 nm), and atomic iron Fe I, which come from the cracking of the ethanol molecules and evaporation of the ultrasonic iron tip surface and electrodes. Also a line of atomic oxygen O I ($\lambda = 777.19$ nm) and molecular spectrum of hydrogen H_2 are also clearly visible. The spectral lines were identified using the data from Refs. 17 and 18.

The process of formation of iron carbide-filled carbon nanocapsules can be envisaged as follows: when iron is evaporated simultaneously with the decomposition of ethanol molecules by the plasma discharge, iron atoms Fe I and carbon species C_2 react with each other and then the iron-carbon alloy particles are formed in close proximity to the plasma discharge zone. These particles may

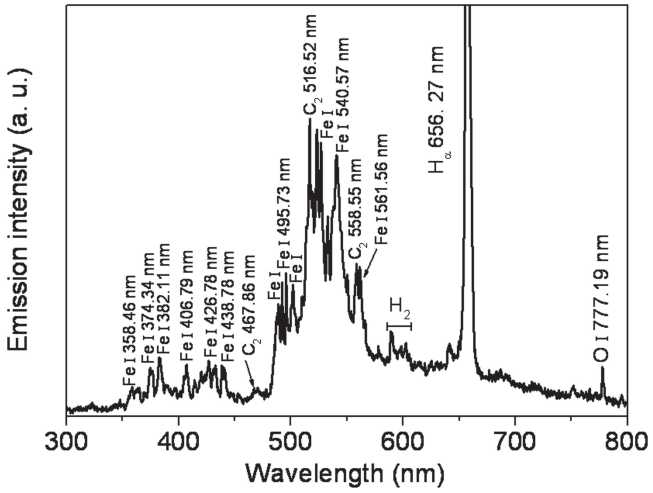

FIG. 6. Optical emission spectrum from plasma discharge of pure ethanol, Fe electrodes, and tip.

be initially liquid, and then, through quenching by the surrounding liquid ethanol, the liquid alloy particles begin to solidify out of the plasma discharge zone. Because the melting point of carbon is much higher than that of iron-carbon alloy, the supersaturated carbon first segregates from the liquid alloy particle during the quenching. Graphite layers are formed on the outer surface of the particle, and thus the iron-carbon alloy particle is entrapped in the core. According to the Fe-C binary phase diagram, the segregation of carbon atoms dissolved in the molten iron-carbon alloy continues until the composition of the alloy reaches to Fe_3C or χ-$Fe_{2.5}C$, which equilibrates with graphite layers on the surface of the carbide nanoparticles. However, some of the cores remained in an amorphous state because of the rapid cooling. In addition, the appearance in the plasma spectrum of intermediate species of the C_2 can be taken as an indication of the formation of solid amorphous carbon.

C. XRD patterns of carbon nanocapsules

To further confirm the phase characterization of the carbon nanocapsules, XRD measurements were conducted. Figure 7 shows the XRD patterns of the samples before annealing and postannealing at various temperatures (673, 873, and 1173 K) for 2 h. The XRD-profile [Fig. 7(a)] of the as-prepared sample powder shows the presence of iron carbides Fe_3C and χ-$Fe_{2.5}C$, and contains a weak peak for the graphitic carbon [$2\theta = 26.44°$, (002) reflection]. The broad peak over the $2\theta = 35$–$50°$ range probably results from some of the synthesized nanoparticles being in an amorphous state in the as-prepared sample. In addition, the small size of the carbon nanocapsules could result in peak broadening. These ideas support our interpretation of the TEM results.

Fully crystallized Fe_3C and α-Fe were then obtained at and above 673 K. After annealing at 673 K for 2 h, the

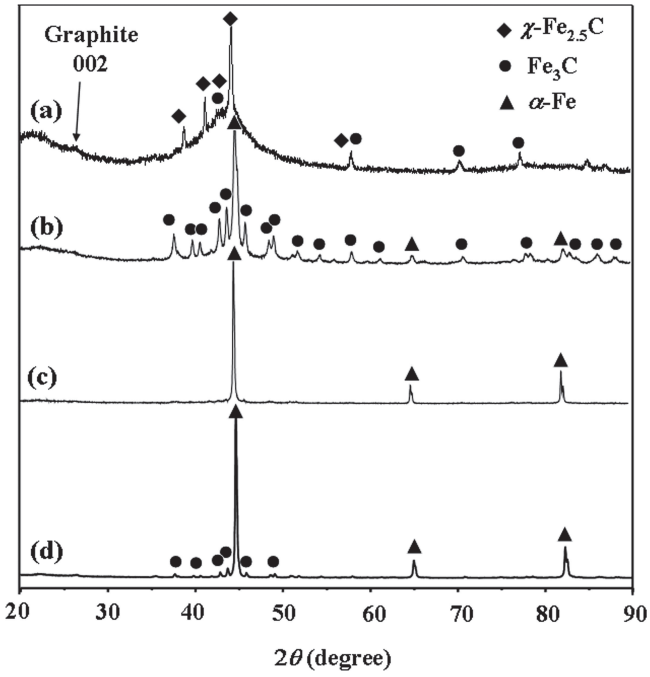

FIG. 7. (a) XRD patterns of powder samples, (b) as-prepared and annealed at 673 K, (c) 873 K, and (d) 1173 K.

cementite peaks coexisted with those of α-Fe, as detected in the XRD pattern [Fig. 7(b)]. At 673 K, iron carbides could not completely decompose into pure iron and graphite; therefore, a noticeable quantity of cementite was contained in the sample. Further heat treatment of the carbon nanocapsules at elevated temperatures as high as 873 and 1173 K [Figs. 7(c) and 7(d)] resulted in iron carbide decomposition, and a large amount of α-Fe was detected in the powder samples. However, traces of cementite that were left intact can be seen from the XRD profile of carbon nanocapsules annealed at 1173 K [Fig. 7(d)]. This is in agreement with the findings of the TEM analysis where small-size cores of carbon nanocapsules were revealed to be in the cementite phase.

D. Magnetic properties

The magnetization and coercivity of the synthesized powder were measured by VSM at room temperature using an applied magnetic field in the range from −1200 to +1200 kA/m. The hysteresis loops of the powder samples annealed at different temperatures are presented in Fig. 8(a). The low field parts of these loops are shown in Fig. 8(b).

The shapes of the hysteresis loops at different annealing temperatures are similar, except for the larger saturation magnetization and coercivity that results from an increase in annealing temperature. All samples showed a ferromagnetic behavior, attaining saturation at 1200 kA/m (Fig. 8) with a low ratio of remanent to saturation

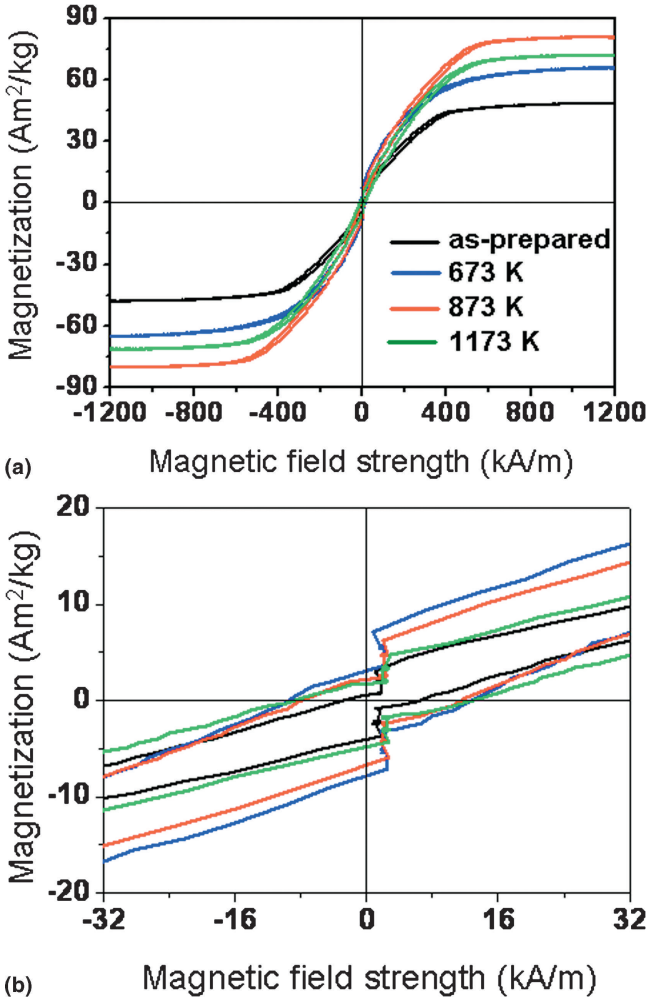

FIG. 8. (a) Hysteresis loops of synthesized powder annealed at different temperatures; (b) the low field parts of the loops shown in (a). The jump in the magnetic hysteresis loops (b) indicates magnetic switching, where the magnetization changes direction.

magnetization, Mr/Ms = 3.7 % for the as-prepared material and 5%–7% (Table I) for the annealed powder samples (this ratio did not change significantly at different annealing temperatures). The low remanence value (Mr/Ms) in the as-prepared and annealed samples can be attributed to a reduction of the interactions between particles with a broad size distribution. The saturation magnetization, Ms, and coercivity, Hc, of the reference powders and all samples are summarized in Table I as a function of annealing temperature. The coercivity of the as-prepared sample was about 4.16 kA/m, and the saturation magnetization was about 48 A m^2/kg at the applied magnetic field of 1200 kA/m. In contrast, the coercivity and saturation magnetization values for a reference crystalline powder of cementite are about 10.42 kA/m and 110 A m^2/kg, respectively. To account for the differences between the magnetic properties of the as-prepared powder and those of the reference iron carbides, we assume that the proportion of nonmagnetic phases (graphite and amorphous carbon) has a detrimental effect on the saturation magnetization and coercivity. Additionally, small {less than 10 nm [Fig. 3(b)]} or amorphous cores may exhibit superparamagnetism and reduce the saturation magnetization and coercivity.

After annealing, the saturation magnetization value and coercivity were raised in comparison with the as-prepared sample. The dependence of magnetic parameters on the annealing temperature is attributed to the change in the particle structure and composition, as well as to the particles' size and their morphology. Various publications[19–21] have shown a distinct increase in the saturation magnetization after annealing at temperatures around or higher than 970 K as cementite decomposition occurred. The maximal values of Ms = 80.6 and 83.4 A m^2/kg in the present samples (Table I) were at 873 and 973 K, respectively, probably the temperatures most favorable for the cementite decomposition into α-Fe and graphite. In addition, particle growth [Figs. 3(c)

TABLE I. Magnetic properties of prepared powder samples.

Samples annealed at different temperatures (K)	Saturation magnetization (Ms, A m^2/kg)	Remanent magnetization (Mr, A m^2/kg)	Remanence (Mr/Ms, %)	Coercivity (Hc, kA/m)
α-Fe[a]	204.0	6.78	3.3	2
Fe_3C[b]	110.0	6.10	5.5	10.42
As-prepared	48.0	1.80	3.75	4.16
573	55.6	3.52	6.33	7.54
673	65.5	4.82	7.36	10.90
773	69.3	4.63	6.68	10.85
873	80.6	3.9	4.84	9.36
973	83.4	4.31	5.17	10.41
1073	79.7	3.57	4.48	11.02
1173	71.7	2.87	4.00	10.64

[a]Reference α-Fe (mean particles size is 45 μm; Wako, purity 99.9%).
[b]Reference cementite (mean particles size is 130.4 μm; Soekawa Chem., purity >96%).

and 3(d)] could also lead to an increase in the saturation magnetization because the number of small particles in a superparamagnetic state was decreased. However, with a further increase in the annealing temperature to 1173 K, the saturation magnetization started to decrease. Such behavior probably relates to the thermodynamic stability of cementite at higher temperatures because an increase in the annealing temperature leads to a rise in the Gibbs free energy of the cementite decomposition reaction. The carbon nanocapsules annealed at 873 and 973 K have 40% of the saturation magnetization value (Table I) of bulk reference α-Fe. As mentioned above, they may incorporate nonmagnetic phases (amorphous carbon and graphite), as well as remaining cementite particles. The elimination of amorphous carbon from the synthesized samples may increase their saturation magnetization.

When the annealing temperatures were 673 and 773 K, the coercivity (*Hc*) drastically increased up to 10.90 and 10.85 kA/m (Table I), respectively, because most of the nanocapsules' cores that were in an amorphous state in the as-prepared sample had been transformed mainly into crystalline cementite. However, at 873 K, the coercivity fell slightly to 9.36 kA/m compared with lower (673 and 773 K) and higher temperatures (1073 and 1173 K). This fact can be attributed to less cementite stability at 873 K and the formation of abundant amount of α-Fe. However, the coercivity of the synthesized samples annealed at elevated temperatures (873–1173 K) was much higher than that of the reference bulk α-Fe as shown in Table I from the nanosized α-Fe cores of the carbon capsules compared with the reference micron-sized α-Fe particles.[22]

IV. CONCLUSION

Carbon-encapsulated iron carbide nanocapsules have been synthesized by a developed method in which ultrasonic cavitation permits an electric plasma discharge to occur at low levels of electric power, even in insulating organic solutions. From the emission spectrum, we could speculate that the formation of carbon nanocapsules occurred from the reaction of atomic iron Fe I with carbon species C_2 and then a molten iron-carbon alloy was transformed during cooling into solid carbides covered with graphite layers.

The as-prepared carbon-encapsulated iron carbide nanoparticles produced by this method ranged in size from several nanometers to 650 nm in diameter. The use of annealing changed the phase composition, structure, and size of the carbon nanocapsules. The iron carbides were mainly transformed into the α-Fe phase at temperature 873 K and above, and their size range increased because of sintering. However, the majority of small-sized (less than 10–20 nm in diameter) cementite nanoparticles did not transform into pure iron, even at high temperatures. After annealing, the values of the saturation magnetization and coercivity of the annealed samples were increased compared with those of the as-prepared sample as a result of phase and size transformations. For technical applications, it is necessary to control the size of synthesized carbon nanocapsules, and any included amorphous carbon needs to be removed.

ACKNOWLEDGMENT

This work was supported by a Grant-in-Aid for Exploratory Research from the Ministry of Education, Culture, Sports, Science and Technology (No. 17656243).

REFERENCES

1. M. Hanayama and T. Ideno: Magnetic recording medium. Japan Patent: JP 06-152793.
2. A.A. Kuznetsov, V.I. Filippov, O.A. Kuznetsov, V.G. Gerlivanov, E.K. Dobrinsky, and S.I. Malashin: New ferro-carbon adsorbents for magnetically guided transport of anti-cancer drugs. *J. Magn. Magn. Mater.* **194,** 22 (1999).
3. Y. Saito, T. Yoshikawa, M. Okuda, N. Fujimoto, K. Sumiyama, K. Suzuki, A. Kasuya, and Y. Nishina: Carbon nanocapsules encaging metals and carbides. *J. Phys. Chem. Solids* **54**(12), 1849 (1993).
4. J. Jiao, S. Seraphin, X. Wang, and J.C. Withers: Preparation and properties of ferromagnetic carbon-coated Fe, Co, and Ni nanoparticles. *J. Appl. Phys.* **80(1),** 103 (1996).
5. R. Sergiienko, E. Shibata, Z. Akase, H. Suwa, T. Nakamura, and D. Shindo: Carbon encapsulated iron carbide nanoparticles synthesized in ethanol by an electric plasma discharge in an ultrasonic cavitation field. *Mater. Chem. Phys.* **98,** 34 (2006).
6. E.A. Neppiras: Acoustic cavitation. *Phys. Rep.* **61,** 159 (1980).
7. Y.T. Didenko, W.B. McNamara III, and K.S. Suslick: Hot spot conditions during cavitation in water. *J. Am. Chem. Soc.* **121,** 5817 (1999).
8. W.B. McNamara III, Y.T. Didenko, and K.S. Suslick: Sonoluminescence temperatures during multi-bubble cavitation. *Nature* **401,** 772 (1999).
9. E. Shibata, R. Sergiienko, H. Suwa, and T. Nakamura: Synthesis of amorphous carbon particles by an electric arc in the ultrasonic cavitation field of liquid benzene. *Carbon* **42,** 885 (2004).
10. R. Sergiienko, E. Shibata, H. Suwa, T. Nakamura, Z. Akase, Y. Murakami, and D. Shindo: Synthesis of amorphous carbon nanoparticles and carbon encapsulated metal nanoparticles in liquid benzene by an electric plasma discharge in ultrasonic cavitation field. *Ultrason. Sonochem.* **13,** 6 (2006).
11. F. Paschen: Über die zum Funkenübergang in Luft, Wasserstoff and Kohlensäure bei verschiedenen Drücken erforderliche Potentialdifferenz. *Weid. Ann. Phys.* **37,** 69 (1889).
12. J. Fuhr, W.F. Schmidt, and S. Sato: Spark breakdown of liquid hydrocarbons. I. Fast current and voltage measurements of the spark breakdown in liquid n-hexane. *J. Appl. Phys.* **59**(11), 3694 (1986).
13. J. Fuhr and W.F. Schmidt: Spark breakdown of liquid hydrocarbons. II. Temporal development of the electric spark resistance in *n*-pentane, *n*-hexane, 2,2 dimethylbutane, and *n*-decane. *J. Appl. Phys.* **59(11),** 3702 (1986).
14. J. Zhang and O. Ostrovski: Cementite formation in CH_4-H_2-Ar gas mixture and cementite stability. *ISIJ Int.* **41(4),** 333 (2001).
15. T. Hayashi, S. Hirono, M. Tomita, and S. Umemura: Magnetic

thin films of cobalt nanocrystals encapsulated in graphite-like carbon. *Nature* **381,** 772 (1996).
16. O. Mamezaki, H. Adachi, S. Tomita, M. Fujii, and S. Hayashi: Thin films of carbon nanocapsules and onion-like graphitic particles prepared by the cosputtering method. *Jpn. J. Appl. Phys.* **39,** 6680 (2000).
17. R.W.B. Pearse and A.G. Gaydon: *The Identification of Molecular Spectra*, 4th ed. (Chapman and Hall, London, 1976).
18. A.R. Striganov and N.S. Sventitskii: *Tables of Spectral Lines of Neutral and Ionized Atoms* (IFI/Plenum, New York, 1968).
19. E.P. Yelsukov, A.I. Ul'yanov, A.V. Zagainov, and N.B. Arsent'yeva: Hysteresis magnetic properties of the Fe(100 – x)C(x); x = 5-25 at.% nanocomposites as-mechanically alloyed and after annealing. *J. Magn. Magn. Mater.* **258-259,** 513 (2003).
20. Z.D. Zhang, J.G. Zheng, I. Skorvanek, J. Kovac, J.L. Yu, X.L. Dong, Z.J. Li, S.R. Jin, X.G. Zhao, and W. Liu: Synthesis, characterization, and magnetic properties of carbon- and boron-oxide-encapsulated iron nanocapsules. *J. Nanosci. Nanotechol.* **1(2),** 153 (2001).
21. T. Hihara, H. Onodera, K. Sumiyama, K. Suzuki, A. Kasuya, Y. Nishina, Y. Saito, T. Yoshikawa, and M. Okuda: Magnetic properties of iron in nanocapsules. *Jpn. J. Appl. Phys.* **33,** L24 (1994).
22. D.L. Leslie-Pelecky and R.D. Rieke: Magnetic properties of nanostructured materials. *Chem. Mater.* **8,** 1770 (1996).